Adaptive Pulse Wave Imaging: automated spatial vessel wall inhomogeneity detection in phantoms and in-vivo

Iason Z. Apostolakis[#1], **Grigorios M. Karageorgos**[#1], **Pierre Nauleau**[1], **Sacha D. Nandlall**[1], **Elisa E. Konofagou**[1,2] **[Member, IEEE]**

[1]Department of Biomedical Engineering, Columbia University, New York, NY, USA

[2]Department of Radiology, Columbia University, New York, NY, USA

[#] These authors contributed equally to this work.

Abstract

Imaging arterial mechanical properties may improve vascular disease diagnosis. Pulse wave velocity (PWV) is a marker of arterial stiffness linked to cardiovascular mortality. Pulse wave imaging (PWI) is a technique for imaging the pulse wave propagation at high spatial and temporal resolution. In this study, we introduce adaptive PWI, a technique for the automated partition of heterogeneous arteries into individual segments characterized by most homogeneous pulse wave propagation, allowing for more robust PWV estimation. This technique was validated in a silicone phantom with a soft-stiff interface. The mean detection error of the interface was 4.67 ± 0.73 mm and 3.64 ± 0.14 mm in the stiff-to-soft and soft-to-stiff pulse wave transmission direction, respectively. This technique was tested in monitoring the progression of atherosclerosis in mouse aortas *in vivo* ($n = 11$). PWV was found to already increase at the early stage of 10 weeks of high-fat diet (3.17 ± 0.67m/sec compared to baseline 2.55 ± 0.47m/sec, $p < 0.05$) and further increase after 20 weeks of high-fat diet (3.76 ± 1.20m/sec). The number of detected segments of the imaged aortas monotonically increased with the duration of high-fat diet indicating an increase in arterial wall property inhomogeneity. The performance of adaptive PWI was also tested in aneurysmal mouse aortas *in vivo*. Aneurysmal boundaries were detected with a mean error of 0.68 ± 0.44mm. Finally, initial feasibility was shown in the carotid arteries of healthy and atherosclerotic human subjects *in vivo* ($n = 3$ each). Consequently, adaptive PWI was successful in detecting stiffness inhomogeneity at its early onset and monitoring atherosclerosis progression *in vivo*.

Keywords

Pulse wave velocity; arterial stiffness; arterial stiffness inhomogeneity; stiffness mapping; atherosclerosis; abdominal aortic aneurysm; graph modeling; silicone phantom

Corresponding author: Elisa E. Konofagou, 351 Engineering Terr., 1210 Amsterdam Ave., New York, NY 10027, ek2191@columbia.edu.

I. INTRODUCTION

Cardiovascular disease (CVD) is a major cause of morbidity and mortality in Western-style populations. Symptomatic large-artery and especially carotid atherosclerosis has been repeatedly linked to an increased risk of stroke [1]. Current clinical tests focus on deriving the degree of stenosis of the affected artery. This parameter though presents limitations, since less stenotic arteries can also lead to stroke events[2]. Additionally, the effectiveness of these tests has not been proven in the detection of early stage subclinical atherosclerosis [3]. Abdominal aortic aneurysm (AAA) is another type of CVD that is a significant cause of morbidity, especially in older populations [4]. The highest risk of rupture is considered when the aneurysmal sac reaches or exceeds 5–5.5cm in diameter or when its maximal diameter increases more than 0.5–1cm within a year [5]. However, it has been previously reported that the size of the aneurysm as a rupture risk assessment criterion is not reliable and does not have a sound theoretical basis [6].

Atherosclerosis and AAAs alter the arterial wall geometry and composition, thus causing changes to its mechanical properties and decreasing the spatial stiffness homogeneity of the diseased vessel, along both the longitudinal and the circumferential axis [7–8]. To monitor these changes, ultrasound imaging, a low cost, noninvasive and easily accessible modality has been the platform on which a multitude of local arterial elasticity imaging techniques have been developed [9]. Vascular Elastography [10–19] Acoustic Radiation Force Imaging (ARFI) [20] and Shear Wave Elastography (SWE) [21–24] are methods that have shown great promise in vascular disease diagnosis by depicting the wall's mechanical properties.

An important parameter used in multiple longitudinal clinical studies as a surrogate measure of stiffness is Pulse Wave Velocity (PWV) [25–26]. PWI is a noninvasive, ultrasound-based technique for tracking the pulse wave propagation and providing a regional PWV estimate along a segment of major arteries at high spatial and temporal resolutions [27–29]. PWI has previously been extended by our group with piecewise PWI (pPWI), enabling imaging and tracking of the pulse wave propagation along a few mm of the arterial wall [30]. Additionally, multiple groups including ours have augmented PWI utilizing high-frame rate plane wave imaging [31–33]. More recently, a Pulse Wave Inverse Problem (PWIP) to estimate the spatially varying arterial PWVs and arterial compliance has been proposed [34]. This method maximized the information used from pulse wave propagation maps and can be used to account for the interference of reflections in the estimation of local PWVs.

However, in piecewise PWI, the size of the PWV segments is fixed and their placement is sequential. This leads to segments spanning across inhomogeneous arterial segments and the corresponding piecewise PWV estimation being compromised due to nonlinear pulse wave propagation, especially in diseased arteries [30]. The more recently developed PWIP, while increasing the level of sophistication in the PWV estimation, still operates in a similar way estimating the local compliances at a fixed equispaced grid of points along the arterial wall with no prior consideration of the underlying mechanical properties. As a result, PWIP compliances tend to have a smoothing effect at transition points where the compliance of the vessel changes rapidly [34].

Previous methodologies to noninvasively capture the spatial variation of the arterial wall's mechanical properties were presented in [7] and [35]. Texture analysis of strain rate images of plaque tissue has indicated that increased local variations in strain rate in plaques may help identify vulnerable plaques [36]. Moreover, earlier work on arterial elastography by Kanai et al. [37] showed increased spatial heterogeneity of the elasticity around plaques, where large stress is concentrated. Finally, previous work by our group has shown that PWI was able to detect increased nonlinearity in the pulse wave propagation in AAAs [28], [38] with unstable aneurysms appearing to be the most inhomogeneous [29]. Moreover, PWI has demonstrated the feasibility to detect calcified plaques in atherosclerotic carotid arteries [39].

Adaptive PWI showcases how an algorithm can utilize the PWI information to identify and monitor arterial abnormalities. The proposed technique was used to automatically detect the soft and stiff segments of silicone phantoms with validation via static testing and its feasibility was tested *in vivo* in monitoring the progression of atherosclerosis in mice and in automatic detection of arterial wall property variation interfaces in aneurysmal mouse aortas. Finally, initial feasibility was shown in three healthy volunteers and three atherosclerotic patients *in vivo*.

II. MATERIALS AND METHODS

A. Silicone Phantom Design

A phantom with a soft and a stiff segment was constructed according to [40], with the stiff segment containing higher concentration of ultrasound scatterers. Static testing was performed similarly to [34],[40] to derive the static PWVs. A hole was made on the top surface of the surrounding material, which was used as reference to identify the stiff-soft interface. Rubber tubes were attached to the ends of the phantom, fixed above the level of the phantom and the resulting system was filled with water, applying a small pre-stretch to the phantom. Pulses were generated by releasing a pinch on one of the rubber tubes.

A quantitative image intensity analysis was carried out in order to verify the position of the stiff-soft interface, as shown in fig. 1-(b)–(d). In each acquired B-mode image, the top wall of the phantom was isolated in a 20 mm long region including the transition. The resulting image of the upper wall segment was then converted into a binary image, by setting all pixels with brightness less than 20% of the brightness range to 0, and the remaining pixels to 1. Subsequently, the number of non-zero pixels was counted in each column (positive pixels per column – ppc (x)), and the resulting vector was smoothed using a second order Savitzky – Golay filter with a Kernel of 13 points. The function ppc(x) quantifies the number of scatterers with respect to the lateral position. Since the stiff segment of the phantom contains higher scatterer concentration, the stiff/soft interface was defined as the lateral position that minimizes the spatial derivative $\frac{d(ppc(x))}{dx}$ This analysis was performed over 8 different acquisitions, and the average position of the interface was determined to be 8.66±0.58 mm away from the hole.

B. Mouse and Human Study design

All procedures performed in the mouse study were approved by the Institutional Animal Care and Use Committee (IACUC) of Columbia University (protocol AC-AAAT6458). For the atherosclerosis study, n=11 (n=7 out of 11 acquisitions were reanalyzed from [30]) six-month old ApoE knockout mice ($ApoE^{-/-}$) were obtained from Jackson Laboratories (Bar Harbor, ME, USA). In order to facilitate atherosclerotic plaque development, they were fed an atherogenic high-fat-type diet (20% protein, 50% carbohydrate, 21% fat, 0.21% cholesterol; Research Diets, New Brunswick, NJ, USA) [41]. One of the acquired mice died after 17 weeks of high-fat diet from myocardial infarction during anesthesia, while two were euthanized due to poor health and deep skin ulcerations after 25 weeks on high-fat diet. The rest of the mouse cohort ($n = 8$) were euthanized after approximately 35 weeks. The abdominal aortas of each mouse were scanned at 0, 10, 20 and 30 weeks after the beginning of the high-fat diet in order to monitor the progression of atherosclerosis.

In the case of the aneurysmal mouse study, n=8 (n=8 out of 8 acquisitions were reanalyzed from [29]) male ApoE/TIMP-1 knockout mice were infused with angiotensin II (A9525, Sigma-Aldrich, St. Louis, MO, USA) for 30 days via subcutaneously implanted osmotic pumps (Alzet Model 2004, Durect, Cupertino, CA, USA) as in [29]. The mice were given a dose of 2.2 mg/kg/day (mg of angiotensin II per kg of body mass per day). These mice were monitored until the formation of a AAA, at which point they were scanned at the aneurysmal location of the abdominal aorta. All procedures pertinent to the human study were approved by the Human Research Protection Office (HRPO) and Institutional Review Boards (IRBs) of Columbia University (protocol AAAR0022). The right common carotids of three male healthy subjects with no prior history of atherosclerosis were scanned (ages: 54, 60 and 73). Additionally, the diseased carotids of three atherosclerotic patients were scanned at the plaque site. More specifically, patient 1 was a 77 y.o. female with the plaque at the right internal carotid close to the bifurcation. Patient 2 was a 62 y.o. female, with the plaque close to the origin of the left internal carotid artery. Finally, patient 3 was a 61 y.o. male with the plaque at the left internal carotid at a site distal to the bifurcation that was more difficult to visualize with ultrasound. In all of the cases, CT angiogram report indicated high grade (70%) stenosis. Information on animal and human studies are summarized in TABLE I.

C. Data acquisition

In the phantom and human subjects, a coherent compounding acquisition sequence with 5 plane waves at angle increments of 1 degree was implemented as in [33]. The plane waves were sent at a pulse repetition frequency of 8333Hz. The sequence was implemented on a Verasonics Vantage 256 system (Verasonics, Kirkland, USA) with a linear array transducer with 128 elements, a central frequency of 5 MHz and a 60% bandwidth (L7–4, ATL Ultrasound, Bothell, WA, USA). In the case of the phantoms, the probe was placed longitudinally along the phantom and care was taken to center around the soft/stiff transition interface. Pulse waves with direction from the soft to the stiff segment as well as from the stiff to the soft segment were generated. In the mouse study, the Vevo 770 high-resolution microscanning system was used (FUJIFILM VisualSonics, Toronto, ON, Canada) connected to a 30MHz single-element transducer (RMV-707B, VisualSonics, Toronto, ON, Canada).

The transducer was placed on the abdomen of the scanned mouse to obtain a longitudinal image of the abdominal aorta. To achieve frame rates in the kHz range, retrospective ECG gating was used [30]. The PRF was 8000Hz at each position and the acquired RF-data were digitized along with the associated ECG signals at 200MHz using a PC with a GaGe digitizer (CompuScope 14200, Gage Applied Technologies, Lachine, QC, Canada). A comparison of the most important parameters of each acquisition is presented in TABLE II.

D. PWI Post Processing

In the case of the phantom and the human subject experiments the channel data were beamformed using a CUDA parallel implementation of a delay-and-sum algorithm (CUDA 6.5, NVIDIA Corporation, Santa Clara, California, U.S.) [33]. The beamformed RF frames from each angle were coherently combined to produce a sequence of compounded RF-frames at 1667 Hz.

Subsequently, the PWI post-processing methodology used for the compounded RF-frames and the synthetic ECG-gated RF-frame sequence was the same. The axial wall displacements were estimated off-line using a GPU-accelerated version of the sum-table 1-D normalized cross-correlation parallelized in [33]. Axial displacements were then normalized (multiplied) by the frame rate producing axial wall velocities (v_{pwi}).

The anterior and posterior walls of the imaged vessel were manually segmented and the v_{pwi} waveforms at each lateral position of these segmentations were sequentially stacked from top (proximal to the pulse wave origin) to bottom (distal to the pulse wave origin). Thus, spatio-temporal maps that depict the v_{pwi} variation over time at each lateral position were generated for each of the anterior and posterior wall segmentations. The two spatio-temporal maps were subtracted and a distension spatio-temporal map was generated, which has been shown to provide more robust PWV estimation [42]. A schematic of the PWI post-processing methodology is shown in Fig. 2.

E. Adaptive PWI methodology

In this section we will describe the methodology employed to detect separated homogeneous segments of the arterial wall by quantifying their pulse wave propagation. Homogeneous pulse wave propagation was evaluated based on two criteria: 1) Linearity of pulse wave propagation within the segment. 2)Homogeneity of peak distension v_{pwi} within the segment. In order to investigate the pulse wave propagation linearity, in the case of the mouse and human studies, the 50% upstroke points of the v_{pwi} versus time were selected as the tracking feature of the pulse wave. This feature has been previously shown to be the most robust compared to other alternatives [43]. In the case of the silicone phantom, releasing a pinch on one of the rubber tubes generated a negative pulse wave and thus a wave with negative v_{pwi} was observed. However, the squeeze-release method generated low v_{pwi} in the stiff segment of the phantom. Consequently, the 50% marker waveform was impacted from increased noise resulting from the susceptibility of low v_{pwi} values to electronic noise [44]. This was confirmed by a previous PWI study, where decreased piecewise r^2 were observed for the lower magnitude v_{pwi} [33]. Thus, the more prominent and relatively higher magnitude feature of the peak negative v_{pwi} was chosen. To model the homogeneity of peak distension,

the peak absolute distension v_{pwi} was estimated at each lateral position from the spatio-temporal map. Subsequently, an optimization algorithm was designed, receiving as inputs the time points of the 50% upstroke markers (MK_i) and the peak distension v_{pwi} (PV_i) at each lateral position ($i = 1...M$ where M is the number of lateral positions) and producing the number, size and position of the segments that are limited by arterial stiffness inhomogeneities and represent the most homogeneous arterial regions. The description of this optimization algorithm is broken into two segments: one describing the modeling of the problem as a graph and one describing the graph solution.

1)   Graph modeling—To solve this optimization problem we chose to model the problem space as a graph as shown in Fig. 3. Each lateral position of the imaged vessel (Fig. 3 (a)) and equivalently of the spatio-temporal map (Fig. 3 (b)) was represented as a node in the graph. Each node was then connected with graph edges (lines in the graph) to nodes corresponding to subsequent lateral positions (Fig. 3 (c)). A numerical value was then linked to each graph edge (graph edge weight). For two nodes corresponding to the lateral positions i and j with $i,j \in [1,M]$ and $i < j$ the weight of the graph edge connecting them w_{ij} is computed as the sum of three metrics as follows:

$$w_{ij} = \widehat{SSE_{MKij}} + \widehat{CV_{PViJ}} + \sqrt[\widehat{L_{ij}}]{\widehat{L_{ij}}} \tag{1}$$

where $\widehat{SSE_{MKij}}$ is the normalized sum of squared errors of the linear fit for all the 50% upstroke markers included between the lateral positions i and j, $\widehat{CV_{PViJ}}$ is the normalized coefficient of variation of the PV_k for all the lateral positions between i and j and $\sqrt[\widehat{L_{ij}}]{\widehat{L_{ij}}}$ is a penalty metric, pertinent the length of the ij segment (L_{ij}). A graphical depiction of each metric is shown in Fig. 4 and a detailed description along with the rationale for each metric is provided in the supplementary files/multimedia tab.

2)   Graph problem solution—Given the modeling described in the previous section, the optimal solution yielding the segmentation of the imaged vessel into segments that are on average the most homogeneous can be represented by the collection of edges ij (or equivalently the path) connecting node 1 to node M with the lowest average of the w_{ij}. If we think of the sum of the w_{ij} of the graph edges included in that path as the paths total distance, then the initial problem can be converted into a modified shortest path-type problem. A simple implementation of a well-known dynamic programming algorithm is, thus, sufficient to solve this problem. More specifically, we implemented a modified version of the established shortest-paths Bellman-Ford algorithm [45]. This algorithm repeats an "edge relaxation" step in which distances to each node are updated with a newly discovered shortest path (details under the supplementary files/multimedia tab). In the present modified implementation, each time an edge relaxation is performed, additionally to the path distance to each node ($\sum_{i, j \in path} w_{ij}$), the number of segments of each path is kept in memory and is used to normalize the distance and thus prevent the algorithm from developing a bias towards paths with a few segments. The number and position of the nodes that are included in the path with the lowest average $w_{ij}\left(\sum_{i, j \in path} w_{ij}\right)$ provides us with the

number and position of the lateral positions between which the arterial segments are most homogeneous.

F. Arterial wall inhomogeneity detection in vivo

In the case of the aneurysmal mouse study, the aim was to investigate whether the aneurysm boundaries (proximal and distal aneurysmal necks), can be identified by adaptive PWI transitions in arterial wall homogeneity. Previous studies have reported stiffness variations between aneurysmal and nonaneurysmal aortic tissue [46],[47]. The first step in detecting the aneurysm boundaries was manual segmentation of the anterior and posterior walls. Subsequently, the vessel diameter was estimated at each lateral position. The location of the maximum diameter waveform was determined followed by the detection of the locations of the maximum second derivative of the diameter on each side of the diameter maximum. These locations were considered to be the ground truth regarding the aneurysm boundaries. A similar approach was use in the case of the atherosclerotic human patients *in vivo*. The plaque boundaries were detected by the locations of the minimum second derivative of the diameter waveform on each side of the diameter minimum.

Repeated measures ANOVA was performed with the Tukey correction for multiple comparisons over the entire mouse population, in order to correlate changes in the number of detected most homogeneous segments and PWV with disease progression.

III.   Results

A. Soft-Stiff Interface Phantom

Fig. 5 shows the spatio-temporal plots and the PWV maps generated for the silicone phantom with the soft and stiff segments. Figs. 5 a) and b) indicate with different colors (pink, blue lines) the segments generated by the adaptive PWI partition for pulse wave propagation from stiff to soft and soft to stiff segments, respectively. Figs. 5 c) and d) provide a visualization of these results (Figs. 5 a) and b) respectively) by color-coding the estimated PWVs and overlaying them onto the B-mode. The interfaces detected by adaptive PWI as well as the soft-stiff interface detected by the B-mode analysis are indicated with dashed lines. Finally, Table III summarized all of the results from four measurements (n=4) for each direction of the pulse wave.

B. Atherosclerotic mouse study

Fig. 6 shows the PWV maps for 3 mice at baseline and after 10, 20 and 30 weeks of high-fat diet. Single-segment segmentation was observed in the case of the baseline PWV maps, indicating smooth pulse wave propagation. Uniform PWV values were found across the baseline mouse aortas. After 10 weeks of high-fat diet, there were either increased PWV values indicating arterial stiffening or increased number of detected segments indicating increased arterial wall inhomogeneity. At 20 weeks, the uniformity of pulse wave propagation was further impacted. Arterial stiffening was observed in several segments with increased PWV. After 30 weeks, vessel fragmentation and segments with increased stiffness persisted, however, several lower stiffness segments were also found.

Fig. 7 shows the mean adaptive PWV and number of detected segments for the entire mouse population. Mean adaptive PWV in baseline aortas (before initiation of the high-fat diet) was 2.55 ± 0.47m/sec ($n = 11$). According to repeated measures ANOVA, significant increase (p 0.05) in the mean adaptive PWV was found after 10 and 20 weeks of high fat diet (3.17 ± 0.67m/sec, $n = 11$ and 3.76 ± 1.20m/sec, $n = 10$ respectively). Mean adaptive PWV dropped after 30 weeks of high-fat diet (2.82 ± 0.74m/sec, $n = 8$). The average baseline number of detected segments was 1.1 ± 0.3 segments ($n = 11$) confirming the homogeneous pulse wave propagation in healthy mouse aortas. An increase in the number of detected segments was found after 10 weeks of high-fat diet (1.9 ± 0.8 segments, $n = 11$) indicating the initial appearance of arterial spatial inhomogeneity. The mouse aortas were found to become less homogeneous after 20 and 30 weeks with significant increases in the number of detected segments compared to the baseline case (2.2 ± 1.1 segments, p 0.05 and 2.75 ± 1.7 segments, p 0.01 respectively).

C. Aneurysmal mouse study

Fig. 8 shows the interfaces detected by adaptive PWI and the boundaries of the aneurysms overlaid onto the B-mode. Table IV summarizes the results of the aneurysmal mouse study. The average distance between each of the aneurysmal boundaries identified through diameter measurement and the closest adaptive PWI interface ($e_{boundary}$) was 0.68 ± 0.44mm, ($n = 8$ mice, $N = 16$ boundaries). Relative error was estimated as $e_{boundary}$ over the corresponding aneurysm length, i.e. the lateral distance between the diameter-based aneurismal boundaries shown in solid blue lines. Finally, the imaged aneurysmal aortas were divided into 3.6 ± 0.5 segments indicating a high degree of inhomogeneity of the afflicted vessel.

D. Atherosclerotic human study

Fig. 9 shows the PWV maps for three healthy volunteers on the top row and three atherosclerotic patients on the second row. Single-segment segmentation was observed in the case of the healthy volunteer PWV maps, indicating smooth pulse wave propagation, and mean adaptive PWVs were found to be 4.70 ± 1.07m/sec. In the case of the atherosclerotic patients more segments were detected (3, 3 and 2 segments for patients 1, 2 and 3, respectively) indicating decreased spatial homogeneity. In the cases of patients 1 and 2 lower PWVs were detected within the segments including the highly stenotic region in each case (0.34m/sec and 1.27m/sec, respectively) while higher PWV was found in the stenotic segment of patient 3 (5.98m/sec). Furthermore, as shown on the third row of Fig. 9 the plaque borders (blue lines) were in the proximity of vessel homogeneity breakpoints detected by adaptive PWI (yellow perforated lines). Mean error between plaque borders and closest adaptive PWI breakpoint was 1.99 ± 0.37mm ($n = 3$ patients, $N = 6$ boundaries) and when compared to the length of the plaque, i.e. the lateral distance between the solid blue lines (mean length: 13.41 ± 4.13mm), the mean relative error was $15.4 \pm 2.0\%$.

IV. DISCUSSION

In the present study, adaptive PWI was introduced as a methodology that combines high spatial and temporal resolution ultrasound imaging with sophisticated graph modeling and

dynamic programming aiming at the automated detection of changes in arterial wall mechanical and geometric properties. It was validated in the case of a phantom with a soft and a stiff segment along the longitudinal axis. Furthermore, its feasibility was tested in monitoring the progression of atherosclerosis in mouse aortas. Its inhomogeneity detection capabilities were tested *in vivo* in the case of aneurysmal mouse aortas against locations of known pulse wave reflection sites, namely the proximal and distal aneurysmal boundaries. Finally, initial results were shown in healthy and atherosclerotic human carotids *in vivo*.

In the case of the silicone phantom study the soft-stiff interface detection error was relatively small ($< 12\%$ of the imaged segment length). Thus, the proposed methodology was able to correctly resolve both the number and the extent of the soft and the stiff phantom segments. Detection errors of the interface can be partly attributed the presence of pulse wave reflections that may disturb the peak distension values proximal to the interface, affecting thus the accuracy of inhomogeneity detection. Future studies will involve investigation of alternative, more robust homogeneity markers, that would minimize detection error.

The estimated adaptive PWVs of the phantom segments were in agreement with the PWV values estimated via static testing. Slightly increased error in the PWV estimation in each case can be found in the first segment in the direction of the pulse wave propagation. This, confirms that PWV estimation is affected in part by the wave reflection at stiffness interfaces. This is in agreement with a study by Latham et al. where the regional PWV measured in the aortic segment preceding the renal branch - a major reflection site - was higher than the expected value and also compared to the PWV measured in the aortic segment immediately following the renal branch, especially in the lower frequencies [48]. Thus, given that wave reflections have been previously reported to impede accurate regional PWV estimation [49][30], the current phantom setup could be potentially very useful in further investigation of the effects of wave reflection on PWV estimation in a controlled environment.

In the case of atherosclerotic mice study, a significant increase in PWV was found at the earliest stage of 10 weeks of high-fat diet, which is the period when the first foam cell lesions start to appear in the mouse aorta [41]. This could have implications for the utility of adaptive PWV in the detection of early stage atherosclerotic disease and also is in agreement with the results of the Rotterdam study where even mild aortic atherosclerosis correlated with elevated levels of aortic PWV [26].This correlation between atherosclerosis and mean adaptive PWV continued into mouse aortas after 20 weeks of high-fat diet. However, it should be noted that after 30 weeks of high-fat diet there was a decrease in mean adaptive PWV. Such a decrease in arterial stiffness in an animal model of prolonged atherosclerosis development has also been reported in a study by Farrar et al. [50] as well as in a previously published piecewise PWI study with a smaller cohort of mice [30] and can be attributed to arterial remodeling and loosening of arterial connective tissue. Lower PWV values may also be associated with possible development of plaques with high lipid necrotic cores, which are characterized by lower stiffness [51]. On the contrary, the number of detected segments monotonically increased as the duration of the high-fat diet increased. Adaptive PWI was, thus, capable of capturing the progression of the level of arterial inhomogeneity due to arterial wall remodeling in atherosclerosis [41],[52].

The aim of the AAA study was to provide an *in vivo* validation of the arterial wall property homogeneity breakpoints detected by adaptive PWI. AAA boundaries have been reported to be sites of variation of the arterial wall's mechanical properties due to differences between the nonaneurysmal and the aneurysmal portions of the aorta in both composition and stiffness [47], [46]. Thus, they are expected to be locations of inhomogeneous pulse wave propagation. Adaptive PWI was shown to be capable of detecting inhomogeneity interfaces in close proximity to the aneurysmal boundaries. By delineating the extent of the aneurysm, adaptive PWI may prove to be especially useful for surgeons planning aortic reconstruction. More specifically, it could be used to complement aortography by providing an objective estimate of the extent of the aneurysm from a biomechanics standpoint, as an alternative to conventional ultrasonography that often yields operator-dependent and imprecise estimates of AAA extent[53].

In the case of the human subjects, increased fragmentation was found in the atherosclerotic patients compared to the healthy subjects. This result was in agreement with the atherosclerosis progression mouse study, indicating more complex wall properties in atherosclerotic carotids. However, it is possible that geometric irregularities due to the presence of a plaque lead adaptive PWI to identify plaque boundaries as points of inhomogeneity. Future studies will involve application of the proposed method in vessel phantoms with embedded plaques of varying stiffness, in order to investigate whether the division of the homogeneous segments is mostly affected by geometry of stiffness variation. Mean adaptive PWVs in healthy subjects were found to be within the physiological range.

In the cases of patients 1 and 2, PWVs were lower within the plaque, while in the case of patient 3, PWV was found to be higher compared to healthy subjects. Such differences in PWV values among subjects can be explained considering that the stiffness of atherosclerotic plaques varies significantly depending on their composition [20][54]. In particular, calcified plaques have been reported to be stiffer than fibrous or non-fibrous tissue [54], while lipid-rich necrotic cores are known to be significantly softer [51].

Additionally, adaptive PWI detected inhomogeneity interfaces in the proximity of the plaque shoulders, which correspond to locations where vessel geometry drastically changes. However, errors between the adaptive PWI interfaces and the AAA or plaque limits did exist (15.4% of plaque/AAA length). A reason for this could be the fact that AAA/plaque limits were estimated merely by a geometrical criterion (diameter waveform). The homogeneity breakpoints detected by adaptive PWI indicate changes not only in diameter but also other factors such as wall thickness and wall structure and composition. Thus, given that adaptive PWI seeks for the location of the most prominent homogeneity breakpoint, the result may differ from the foot of the diameter waveform. Moreover, errors may be present in plaque/ aneurysm border detection, due to noise introduced by the use of a second derivative operator on the diameter measurements.

The effect of pulse wave reflections with respect to geometric and stiffness variations in piecewise (PWV) estimation is a matter that needs to be further investigated. The intensity of a reflected wave is described by the reflection coefficient, which is a function of the transition in vessel's cross sectional area and mechanical properties. It has been shown that

different values of reflection coefficient introduce different biases in PWV estimation [55]. Therefore, PWV values provided by adaptive PWI at each most homogeneous segment may be affected by errors, which are dependent on the size and composition of the aneurysm/plaque. A step towards addressing this limitation would be to combine adaptive PWI with a more robust method for arterial wall characterization, such as the pulse wave inverse problem (PWIP) [34], or cross correlation-based PWI, which account for reflections [40]. In particular, adaptive PWI can be used as a pre-processing step to identify reflection sites and isolate the segments with most homogeneous pulse wave propagation, in which PWIP will be applied.Thus, PWIP will also benefit as it will account for these reflection sites and will be prevented from smoothing out arterial wall inhomogeneities.

Ongoing work involves comparison of the performance of the proposed technique with other ultrasound elasticity imaging methods in vessel wall property characterization, such as NonInvasive Vascular Elastography (NIVE) [13–18] and Shear Wave Elastography (SWE) [21–24]. An advantage of adaptive PWI over SWE is that it exploits the physiological arterial wall motion, instead of relying on application of external ultrasound radiation force, which may increase the complexity of ultrasound acquisition. Moreover, it involves simple arterial wall segmentation which generates only two lines, instead of defining 2-D regions of interest, which can be challenging when plaques are present. However, NIVE and SWE offer the advantage of higher resolution 2-D depiction of tissue mechanical properties. It yet remains to test adaptive PWI in a larger cohort of patients, in order to determine whether it can provide additional critical information, and contribute to vascular disease diagnosis and monitoring.

V. Conclusion

Adaptive PWI, a method of automatically detecting the optimal partition of the arterial wall into homogeneous segments was introduced in this study. Arterial stiffness interfaces, were successfully detected in a silicone phantom with soft and stiff segments. This methodology was also capable of effectively monitoring the progression of atherosclerotic and aneurysmal mouse aortas from the earliest to the latest stages of the disease. Testing of the accuracy of the detected interfaces was performed by automatically detecting the proximal and distal boundaries of AAAs, which are known to be sites of arterial inhomogeneity, in mouse aortas *in vivo*. Finally, preliminary feasibility was shown in healthy and atherosclerotic human subjects.

Supplementary Material

Refer to Web version on PubMed Central for supplementary material.

ACKNOWLEDGEMENT

REFERENCES

[1]. Golledge J, Greenhalgh RM, and Davies AH, "The Symptomatic Carotid Plaque," Stroke, vol. 31, no. 3, pp. 774–781, 3 2000. [PubMed: 10700518]

[2]. Saam T et al., "The Vulnerable, or High-Risk, Atherosclerotic Plaque: Noninvasive MR Imaging for Characterization and Assessment," Radiology, vol. 244, no. 1, pp. 64–77, 7 2007. [PubMed: 17581895]

[3]. Fernández-Ortiz A et al., "The Progression and Early detection of Subclinical Atherosclerosis (PESA) study: Rationale and design," Am. Heart J, vol. 166, no. 6, pp. 990–998, 12 2013. [PubMed: 24268213]

[4]. Hirsch AT et al., "ACC/AHA 2005 Practice Guidelines for the Management of Patients With Peripheral Arterial Disease (Lower Extremity, Renal, Mesenteric, and Abdominal Aortic)," Circulation, vol. 113, no. 11, 3 2006.

[5]. Sakalihasan N, Limet R, and Defawe O, "Abdominal aortic aneurysm," Lancet, vol. 365, no. 9470, pp. 1577–1589, Apr. 2005. [PubMed: 15866312]

[6]. Vorp DA, "Biomechanics of abdominal aortic aneurysm.," J. Biomech, vol. 40, no. 9, pp. 1887–902, 2007. [PubMed: 17254589]

[7]. Meinders J, Brands P, Willigers J, Kornet L, and Hoeks AP, "Assessment of the spatial homogeneity of artery dimension parameters with high frame rate 2-D B-mode," Ultrasound Med. Biol, vol. 27, no. 6, pp. 785–794, Jun. 2001. [PubMed: 11516538]

[8]. Tsamis A, Krawiec JT, and Vorp DA, "Elastin and collagen fibre microstructure of the human aorta in ageing and disease: a review," J. R. Soc. Interface, vol. 10, no. 83, pp. 20121004–20121004, Mar. 2013.

[9]. de Korte CL, Fekkes S, Nederveen AJ, Mannesing R, and Hansen HRHG, "Review: Mechanical Characterization of Carotid Arteries and Atherosclerotic Plaques," IEEE Trans. Ultrason. Ferroelectr. Freq. Control, vol. 63, no. 10, pp. 1613–1623, Oct. 2016. [PubMed: 27249826]

[10]. Hansen HHG, De Borst GJ, Bots ML, Moll F, Pasterkamp G, and De Korte CL, "Noninvasive compound ultrasound elastography for vulnerable plaque detection: in vivo validation," Eur. Heart J, vol. 34, no. suppl 1, pp. P258–P258, Aug. 2013.

[11]. Hansen HHG, de Borst GJ, Bots ML, Moll FL, Pasterkamp G, and de Korte CL, "Compound Ultrasound Strain Imaging for Noninvasive Detection of (Fibro)Atheromatous Plaques: Histopathological Validation in Human Carotid Arteries," JACC Cardiovasc. Imaging, vol. 9, no. 12, pp. 1466–1467, Dec. 2016. [PubMed: 27931528]

[12]. Hansen HHG, de Borst GJ, Bots ML, Moll FL, Pasterkamp G, and de Korte CL, "Validation of Noninvasive In Vivo Compound Ultrasound Strain Imaging Using Histologic Plaque Vulnerability Features," Stroke, vol. 47, no. 11, pp. 2770–2775, Nov. 2016. [PubMed: 27686104]

[13]. Schmitt C, Soulez G, Maurice RL, Giroux M-F, and Cloutier G, "Noninvasive Vascular Elastography: Toward A Complementary Characterization Tool of Atherosclerosis in Carotid Arteries," Ultrasound Med. Biol, vol. 33, no. 12, pp. 1841–1858, Dec. 2007. [PubMed: 17698283]

[14]. Roy Cardinal M-H et al., "Carotid Artery Plaque Vulnerability Assessment Using Noninvasive Ultrasound Elastography: Validation With MRI," Am. J. Roentgenol, vol. 209, no. 1, pp. 142–151, Jul. 2017. [PubMed: 28639927]

[15]. El Jalbout R et al., "The value of non-invasive vascular elastography (NIVE) in detecting early vascular changes in overweight and obese children," Eur. Radiol, vol. 29, no. 7, pp. 3854–3861, Jul. 2019. [PubMed: 30847591]

[16]. Salloum E et al., "Endovascular Repair of Abdominal Aortic Aneurysm: Follow-up with Noninvasive Vascular Elastography in a Canine Model," Radiology, vol. 279, no. 2, pp. 410–419, 5 2016. [PubMed: 26690905]

[17]. Poree J, Garcia D, Chayer B, Ohayon J, and Cloutier G, "Noninvasive Vascular Elastography With Plane Strain Incompressibility Assumption Using Ultrafast Coherent Compound Plane Wave Imaging," IEEE Trans. Med. Imaging, vol. 34, no. 12, pp. 2618–2631, Dec. 2015. [PubMed: 26625341]

[18]. Schmitt C, Soulez G, Maurice RL, Giroux M-F, and Cloutier G, "Noninvasive Vascular Elastography: Toward A Complementary Characterization Tool of Atherosclerosis in Carotid Arteries," Ultrasound Med. Biol, vol. 33, no. 12, pp. 1841–1858, Dec. 2007. [PubMed: 17698283]

[19]. Naim C et al., "Characterisation of carotid plaques with ultrasound elastography: feasibility and correlation with high-resolution magnetic resonance imaging," Eur. Radiol, vol. 23, no. 7, pp. 2030–2041, Jul. 2013. [PubMed: 23417249]

[20]. Czernuszewicz TJ et al., "Non-invasive in Vivo Characterization of Human Carotid Plaques with Acoustic Radiation Force Impulse Ultrasound: Comparison with Histology after Endarterectomy," Ultrasound Med. Biol, vol. 41, no. 3, pp. 685–697, Mar. 2015. [PubMed: 25619778]

[21]. Garrard J et al., "Shear Wave Elastography May Be Superior to Greyscale Median for the Identification of Carotid Plaque Vulnerability: A Comparison with Histology," Ultraschall der Medizin - Eur. J. Ultrasound, vol. 36, no. 04, pp. 386–390, Jun. 2015.

[22]. V Ramnarine K, Garrard JW, Kanber B, Nduwayo S, Hartshorne TC, and Robinson TG, "Shear wave elastography imaging of carotid plaques: feasible, reproducible and of clinical potential," Cardiovasc. Ultrasound, vol. 12, no. 1, p. 49, Dec. 2014. [PubMed: 25487290]

[23]. Widman E, Maksuti E, Larsson D, Urban MW, Bjällmark A, and Larsson M, "Shear wave elastography plaque characterization with mechanical testing validation: a phantom study," Phys. Med. Biol, vol. 60, no. 8, pp. 3151–3174, Apr. 2015. [PubMed: 25803520]

[24]. Bertrand-Grenier A et al., "Abdominal aortic aneurysm follow-up by shear wave elasticity imaging after endovascular repair in a canine model Abbreviations AAA Abdominal aortic aneurysm CEUS Contrast-enhanced ultrasonography CI Confidence interval CT Computed tomography," Eur Radiol, vol. 27, pp. 2161–2169, 2017. [PubMed: 27572808]

[25]. Laurent S et al., "Expert consensus document on arterial stiffness: methodological issues and clinical applications," Eur. Heart J, vol. 27, no. 21, pp. 2588–2605, Sep. 2006. [PubMed: 17000623]

[26]. van Popele NM et al., "Association between arterial stiffness and atherosclerosis: the Rotterdam Study.," Stroke, vol. 32, no. 2, pp. 454–60, Feb. 2001. [PubMed: 11157182]

[27]. Fujikura K et al., "A Novel Noninvasive Technique for Pulse-Wave Imaging and Characterization of Clinically-Significant Vascular Mechanical Properties In Vivo," Ultrason. Imaging, vol. 29, no. 3, pp. 137–154, Jul. 2007. [PubMed: 18092671]

[28]. Luo Jianwen, Fujikura K, Tyrie LS, Tilson MD, and Konofagou EE, "Pulse Wave Imaging of Normal and Aneurysmal Abdominal Aortas In Vivo," IEEE Trans. Med. Imaging, vol. 28, no. 4, pp. 477–486, Apr. 2009. [PubMed: 19272985]

[29]. Nandlall SD and Konofagou EE, "Assessing the Stability of Aortic Aneurysms with Pulse Wave Imaging.," Radiology, vol. 281, no. 3, pp. 772–781, Dec. 2016. [PubMed: 27276242]

[30]. Apostolakis IZ, Nandlall SD, and Konofagou EE, "Piecewise Pulse Wave Imaging (pPWI) for Detection and Monitoring of Focal Vascular Disease in Murine Aortas and Carotids In Vivo," IEEE Trans. Med. Imaging, vol. 35, no. 1, pp. 13–28, Jan. 2016. [PubMed: 26168432]

[31]. Kruizinga P et al., "High-Definition Imaging of Carotid Artery Wall Dynamics," Ultrasound Med. Biol, vol. 40, no. 10, pp. 2392–2403, Oct. 2014. [PubMed: 25088760]

[32]. Hasegawa H, Hongo K, and Kanai H, "Measurement of regional pulse wave velocity using very high frame rate ultrasound," J. Med. Ultrason, vol. 40, no. 2, pp. 91–98, Apr. 2013.

[33]. Apostolakis IZ, McGarry MDJ, Bunting EA, and Konofagou EE, "Pulse wave imaging using coherent compounding in a phantom and in vivo," Phys. Med. Biol, vol. 62, no. 5, pp. 1700–1730, Mar. 2017. [PubMed: 28002039]

[34]. Mcgarry M, Li R, Apostolakis I, Nauleau P, and Konofagou EE, "An inverse approach to determining spatially varying arterial compliance using ultrasound imaging.," Phys. Med. Biol, vol. 61, no. 15, pp. 5486–507, 2016. [PubMed: 27384105]

[35]. Reneman RS, van Merode T, Brands PJ, and Hoeks AP, "Inhomogeneities in arterial wall properties under normal and pathological conditions.," J. Hypertens. Suppl, vol. 10, no. 6, pp. S35–9, Aug. 1992.

[36]. Huang C et al., "Non-Invasive Identification of Vulnerable Atherosclerotic Plaques Using Texture Analysis in Ultrasound Carotid Elastography: An In Vivo Feasibility Study Validated by Magnetic Resonance Imaging," Ultrasound Med. Biol, vol. 43, no. 4, pp. 817–830, Apr. 2017. [PubMed: 28153351]

[37]. Kanai H, Hasegawa H, and Nakagawa N, "Elasticity imaging of atheroma with transcutaneous ultrasound both in longitudinal-axis and short-axis planes," Int. Congr. Ser, vol. 1274, pp. 64–74, Oct. 2004.

[38]. Li RX, Luo J, Balaram SK, Chaudhry FA, Shahmirzadi D, and Konofagou EE, "Pulse wave imaging in normal, hypertensive and aneurysmal human aortas in vivo: a feasibility study," Phys. Med. Biol, vol. 58, no. 13, pp. 4549–4562, Jul. 2013. [PubMed: 23770991]

[39]. Li RX et al., "Pulse Wave Imaging in Carotid Artery Stenosis Human Patients in Vivo.," Ultrasound Med. Biol, vol. 0, no. 0, Nov. 2018.

[40]. Nauleau P, Apostolakis I, McGarry M, and Konofagou E, "Cross-correlation analysis of pulse wave propagation in arteries: In vitro validation and in vivo feasibility," Phys. Med. Biol, vol. 63, no. 11, p. 115006, 5 2018.

[41]. Nakashima Y, Plump AS, Raines EW, Breslow JL, and Ross R, "ApoE-deficient mice develop lesions of all phases of atherosclerosis throughout the arterial tree.," Arterioscler. Thromb. A J. Vasc. Biol, vol. 14, no. 1, pp. 133–140, Jan. 1994.

[42]. Huang C, Su Y, Zhang H, Qian L-X, and Luo J, "Comparison of Different Pulse Waveforms for Local Pulse Wave Velocity Measurement in Healthy and Hypertensive Common Carotid Arteries in Vivo," Ultrasound Med. Biol, vol. 42, no. 5, pp. 1111–1123, 5 2016. [PubMed: 26924694]

[43]. Li RX, Qaqish W, and Konofagou EE, "Performance assessment of pulse wave imaging using conventional ultrasound in canine aortas ex vivo and normal human arteries in vivo," Artery Res, vol. 11, pp. 19–28, Sep. 2015. [PubMed: 26640603]

[44]. Bunting EA, Provost J, and Konofagou EE, "Stochastic precision analysis of 2D cardiac strain estimation in vivo," Phys. Med. Biol, vol. 59, no. 22, pp. 6841–6858, Nov. 2014. [PubMed: 25330746]

[45]. Bellman R, "On a routing problem," Q. Appl. Math, vol. 16, no. 1, pp. 87–90, Apr. 1958.

[46]. He CM and Roach MR, "The composition and mechanical properties of abdominal aortic aneurysms," J. Vasc. Surg, vol. 20, no. 1, pp. 6–13, Jul. 1994. [PubMed: 8028090]

[47]. Thubrikar MJ, Labrosse M, Robicsek F, Al-Soudi J, and Fowler B, "Mechanical properties of abdominal aortic aneurysm wall.," J. Med. Eng. Technol, vol. 25, no. 4, pp. 133–42. [PubMed: 11601439]

[48]. Latham RD, Westerhof N, Sipkema P, Rubal BJ, Reuderink P, and Murgo JP, "Regional wave travel and reflections along the human aorta: a study with six simultaneous micromanometric pressures.," Circulation, vol. 72, no. 6, pp. 1257–1269, Dec. 1985. [PubMed: 4064270]

[49]. Hermeling E, Reesink KD, Reneman RS, and Hoeks AP, "Confluence of incident and reflected waves interferes with systolic foot detection of the carotid artery distension waveform," J. Hypertens, vol. 26, no. 12, pp. 2374–2380, Dec. 2008. [PubMed: 19008715]

[50]. Farrar DJ, Bond MG, Riley WA, and Sawyer JK, "Anatomic correlates of aortic pulse wave velocity and carotid artery elasticity during atherosclerosis progression and regression in monkeys.," Circulation, vol. 83, no. 5, pp. 1754–1763, 5 1991. [PubMed: 2022028]

[51]. Ohayon J et al., "Necrotic core thickness and positive arterial remodeling index: emergent biomechanical factors for evaluating the risk of plaque rupture.," Am. J. Physiol. Heart Circ. Physiol, vol. 295, no. 2, pp. H717–27, Aug. 2008. [PubMed: 18586893]

[52]. Reddick RL, Zhang SH, and Maeda N, "Atherosclerosis in mice lacking apo E. Evaluation of lesional development and progression.," Arterioscler. Thromb. A J. Vasc. Biol, vol. 14, no. 1, pp. 141–147, Jan. 1994.

[53]. "Desforges JF and Ernst CB, 'Abdominal Aortic Aneurysm,' N. Engl. J. Med, vol. 328, no. 16, pp. 1167–1172, 4 1993." [PubMed: 8455684]

[54]. Lee RT et al., "Prediction of mechanical properties of human atherosclerotic tissue by high-frequency intravascular ultrasound imaging. An in vitro study.," Arterioscler. Thromb. A J. Vasc. Biol, vol. 12, no. 1, pp. 1–5, Jan. 1992.

[55]. Borlotti A, Li Y, Parker KH, and Khir AW, "Experimental evaluation of local wave speed in the presence of reflected waves.," J. Biomech, vol. 47, no. 1, pp. 87–95, Jan. 2014. [PubMed: 24252610]
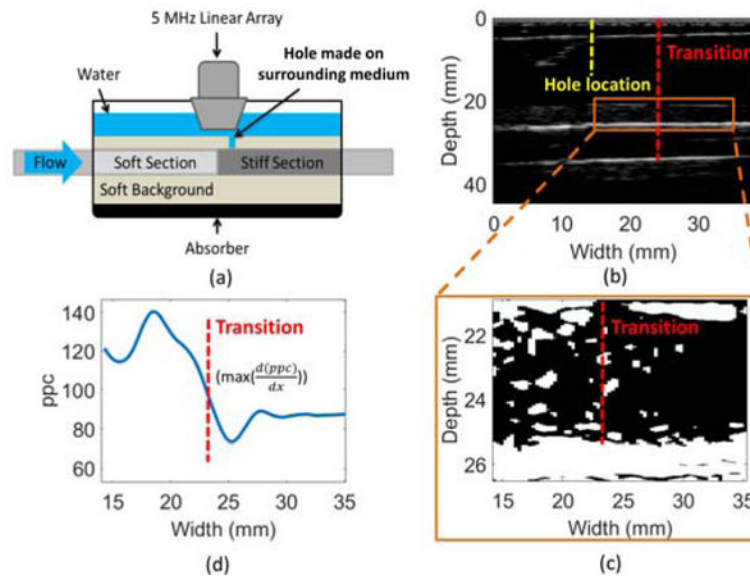
Fig. 1:
(a) Phantom experimental Setup. (b) Acquired B-mode image. The brown rectangle illustrates the segment of the anterior wall which was selected to identify the stiffness transition. (c) Binary image obtained after thresholding the selected anterior wall segment. (d) Function of positive pixels per column (ppc(x)), which quantifies ultrasound scatterer concentration with respect to the lateral position in the selected region of the anterior phantom wall.
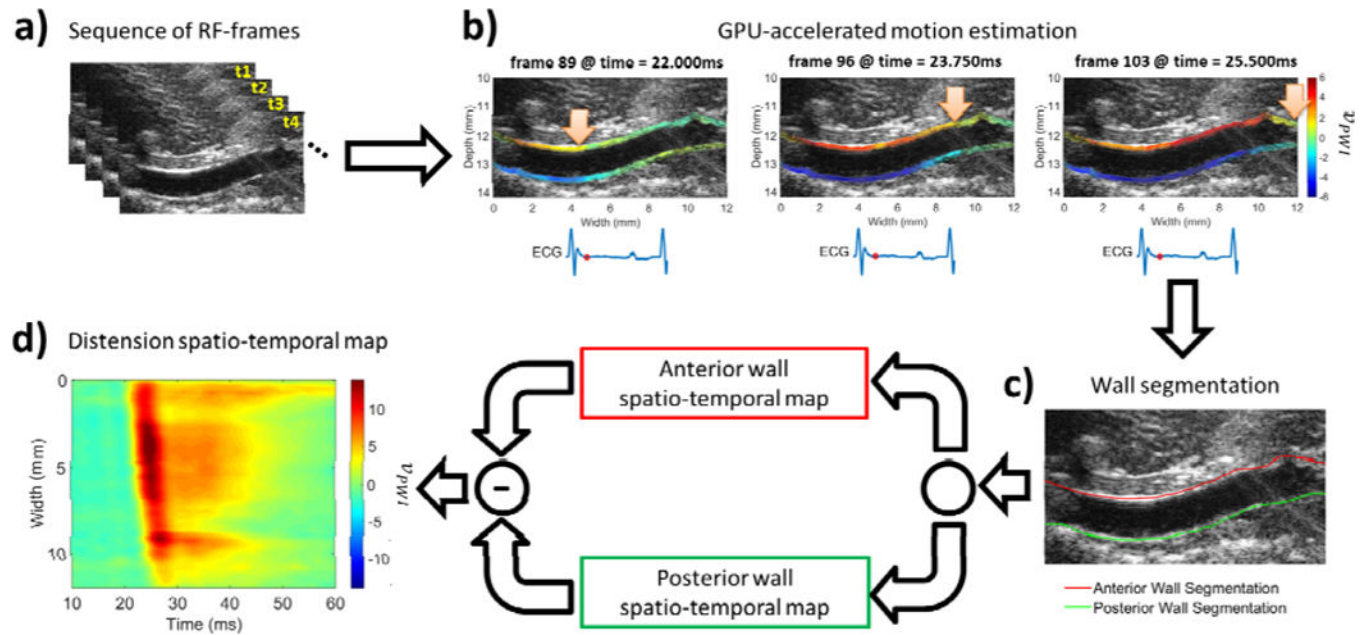
Fig. 2.
PWI post-processing methodology. a) Generated sequence of RF-frames, b) Sequence of B-modes with color-coded and overlaid V_{PWI}. Red indicates motion towards the transducer (upward) and blue indicates motion away from the transducer (downward). c) B-mode with the anterior and posterior walls segmentations (red: anterior wall, green: posterior wall). The orange arrows indicate the approximate location of the pulse wave wavefont at each frame as it propagates from left to right. Time indicates time after the R-peak of the ECG signal. d) Distension spatio-temporal map generated from the subtraction of the anterior and posterior wall spatio-temporal maps. In the figures above, a normal mouse aorta was used as a post-processing example.
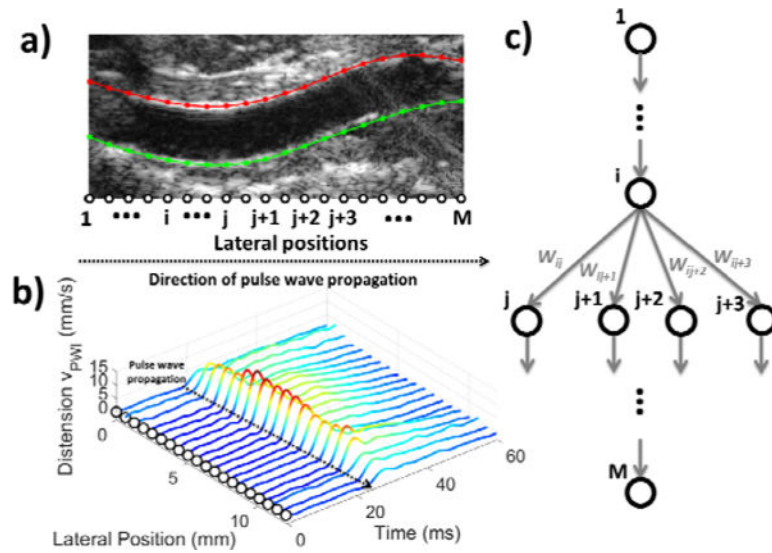
Fig. 3.
Graph modeling of the PWI problem space. a) Segmentation of the anterior and posterior arterial wall of a mouse aorta corresponding to each lateral position. b) Distension v_{PWI} waveforms corresponding to each lateral position of the aorta as indicated in a). c) Graph model of the PWI problem space with each node corresponding to each lateral positions connected with appropriately weighted graph edges.
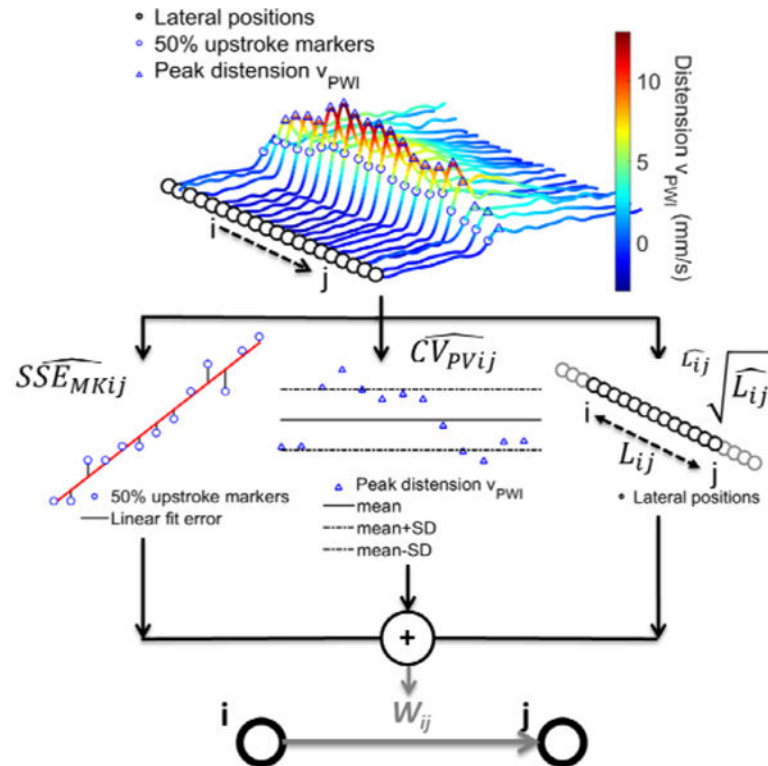
Fig. 4.
Graphical depiction of the metrics used for the edge weight estimation.
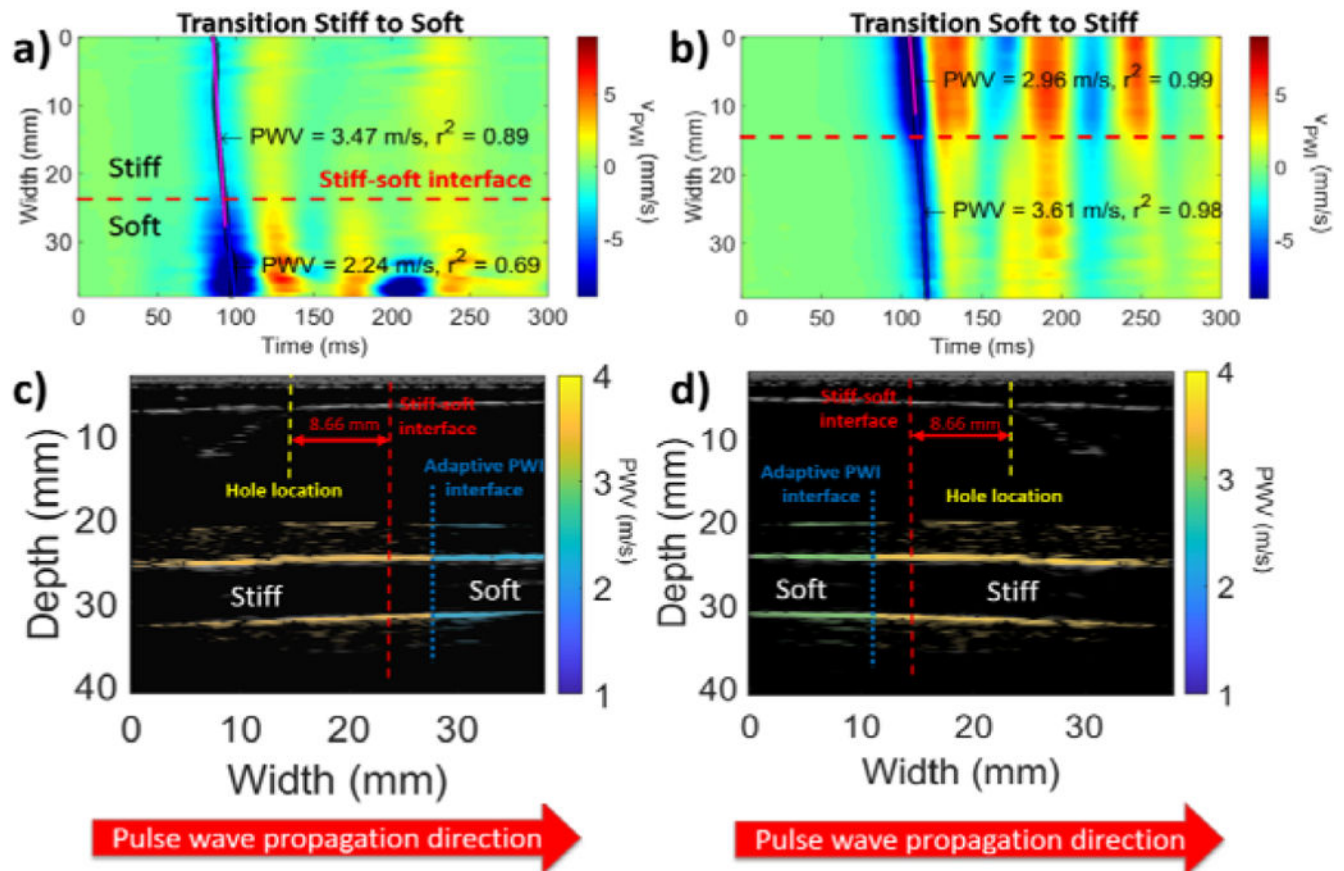
Fig. 5.
a), b) Spatio-temporal plots with the linear regressions generated by adaptive PWI for each propagation direction.The interface location based on B-mode analysis is shown with a perforated red line. c), d) B-modes with the PWV velocities color-coded and overlaid onto the vessel walls for each propagation direction. The soft-stiff interface detected with adaptive PWI is denoted by the vertical dotted blue line, the location of the marking in the surrounding material is indicated with a perforated yellow line and subsequently the location of the interface detected via B-mode analysis is indicated with a perforated red line.
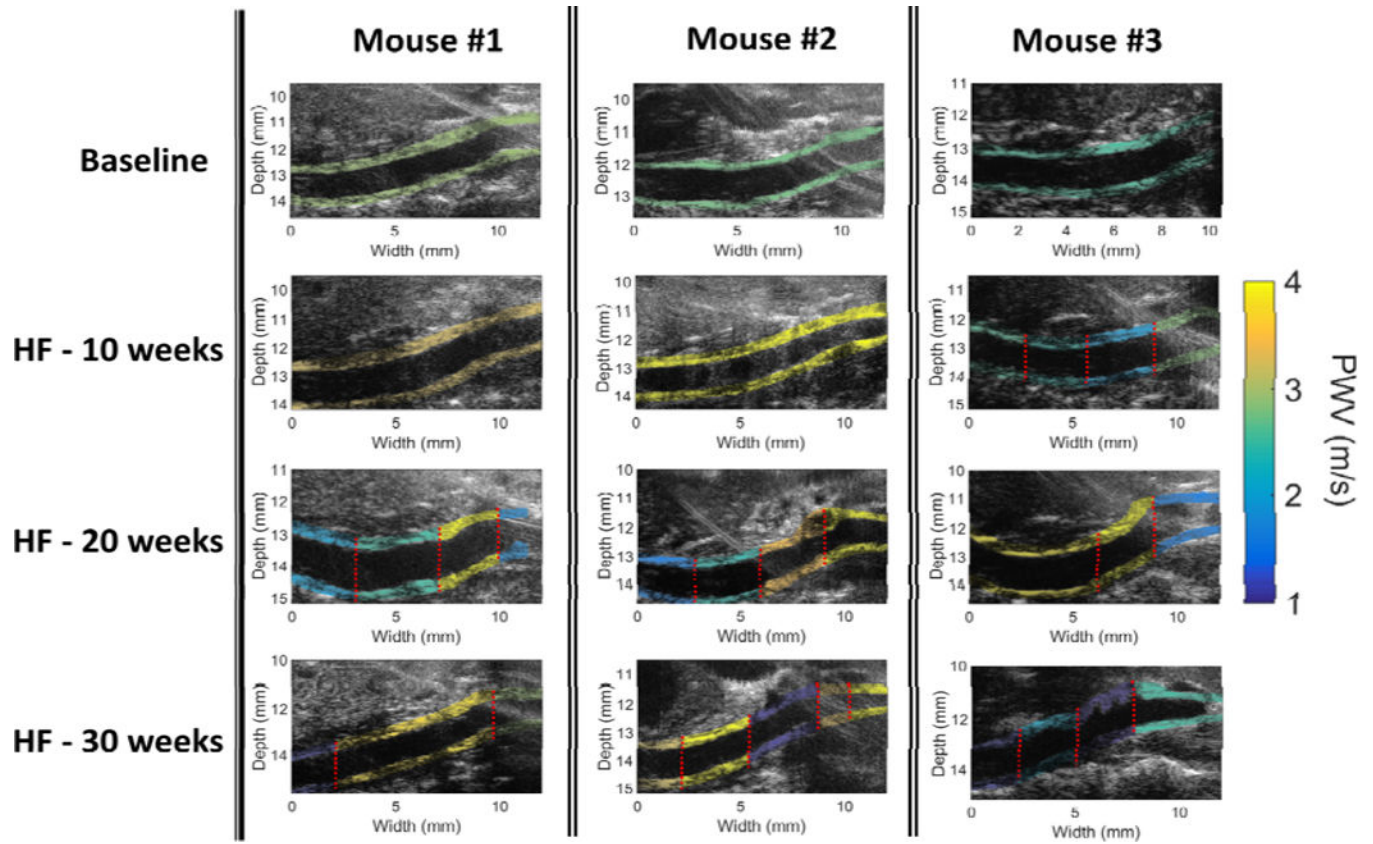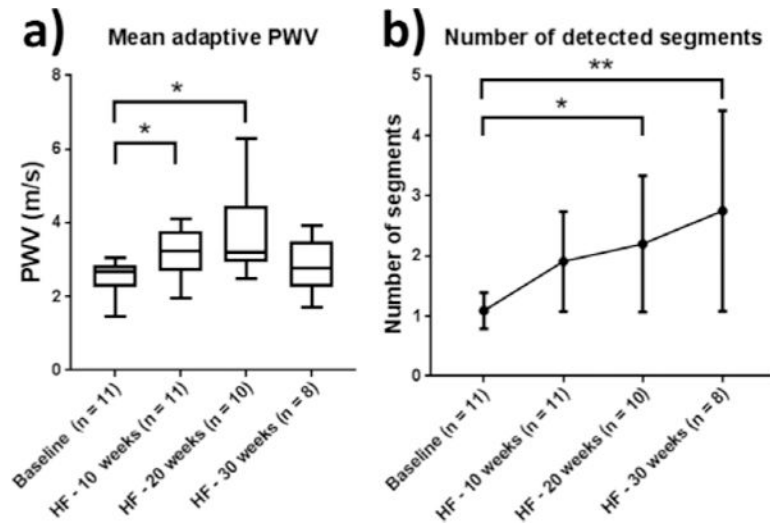
Fig. 6.
PWV maps of three mice at baseline and after 10, 20 and 30 weeks of high-fat diet (HF) the detected interfaces between adaptive PWI segments are indicated with dotted red lines.

Fig. 7.
Atherosclerotic mouse aortas study statistical results. a) Mean adaptive PWV of atherosclerotic mouse aortas at baseline, after 10, 20 and 30 weeks of high-fat diet (HF). b) Mean number of segments detected with adaptive PWI indicating the level of inhomogeneity of the artery at baseline, after 10, 20 and 30 weeks of high-fat diet (HF).
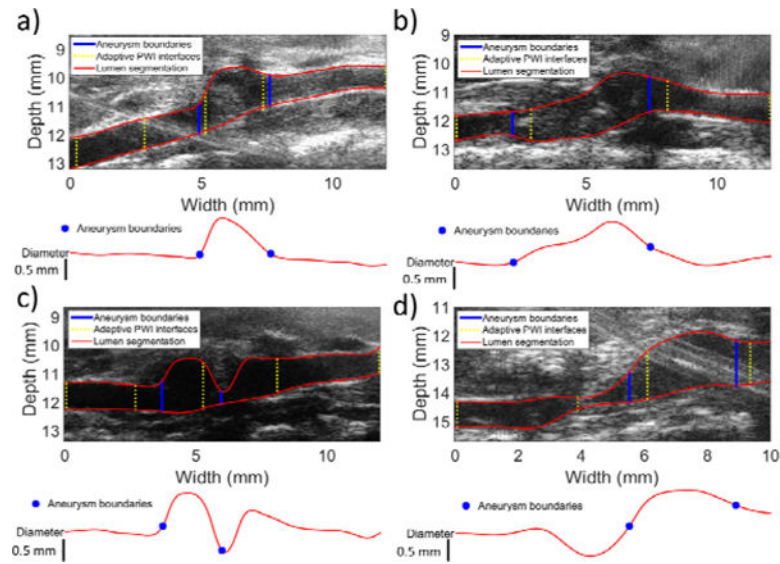
Fig. 8.
a), b), c), d) Inhomogeneity interfaces detected by adaptive PWI (perforated yellow lines), aneurysm boundaries detected with the diameter waveform (blue lines) and lumen segmentation (red lines) overlaid onto the corresponding B-modes of four aneurysmal mouse aortas. Below each B-mode, the corresponding diameter waveform is shown along with the detected aneurysm boundaries (blue points).
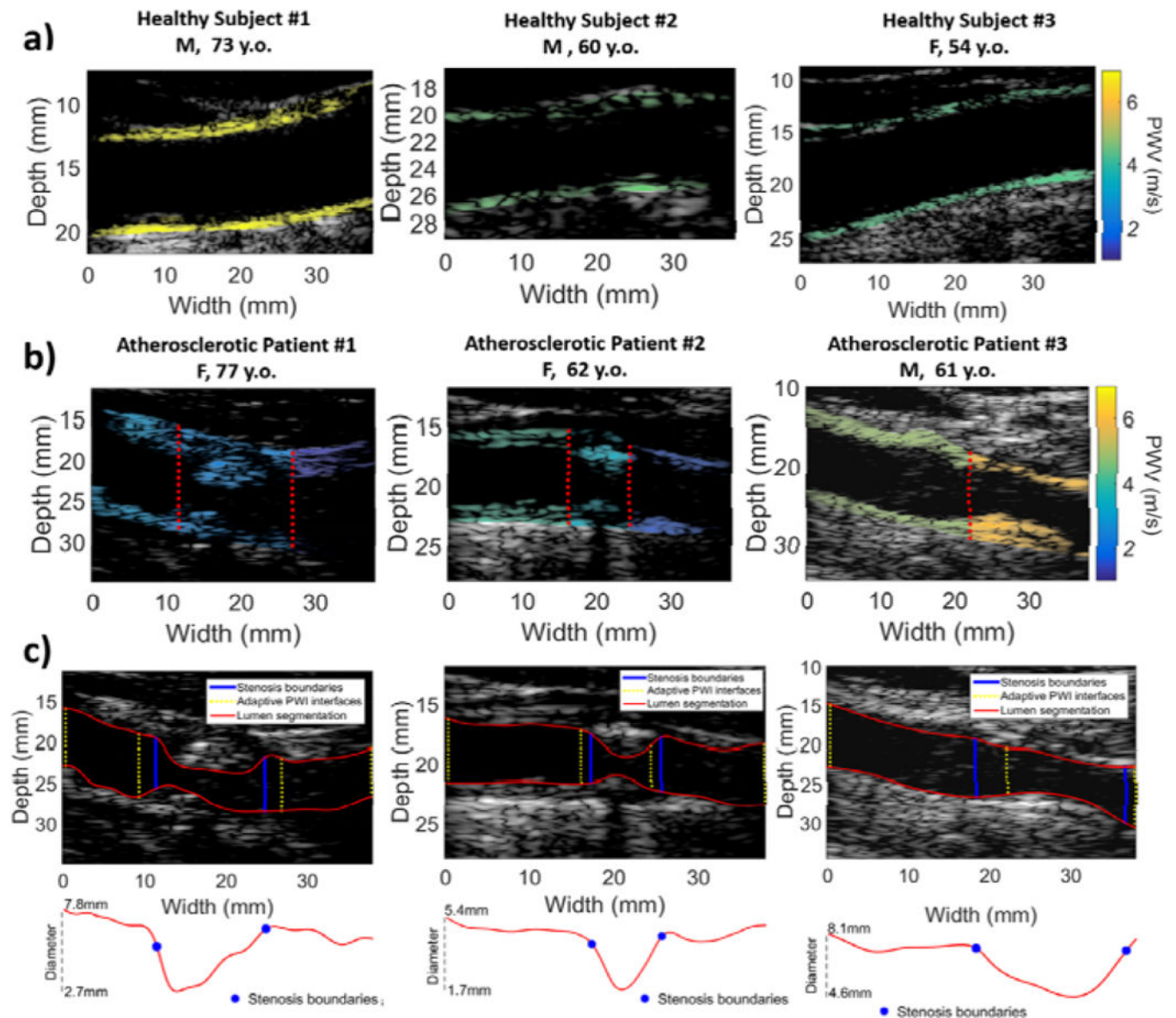
Fig. 9.
a) PWV maps for three healthy volunteers. A single segment was detected in all three cases.
b) PWV maps for three atherosclerotic patients, red perforated lines indicate stiffness
interfaces between the detected segments. c) stiffness interfaces (perforated yellow lines),
plaque boundaries detected with the diameter waveform (blue lines) and lumen segmentation
(red lines) overlaid into the corresponding B-modes of the three atherosclerotic patients.
Below each B-mode the corresponding diameter waveform is shown along with the detected
plaque boundaries (blue points).

TABLE I –

MOUSE AND HUMAN STUDY DESIGN SUMMARY

	Mouse study	
	Atherosclerotic mice	**Aneurysmal mice**
Sample Size	11 (7 out of 11 were reanalyzed [30])	8 (8 out of 8 were reanalyzed from [29])
Duration	30 weeks	30 days
Scanning Timepoints	Once every 10 weeks	2–3 weekly scans
	Human Study	
	Atherosclerotic	Normal Controls
Sample Size	3	3
Age	61–77	54–73
Gender	(2 F, 1 M)	M

TABLE II –

EXPERIMENTAL SETUPS

	Phantom/Human study	**Mouse study**
System	Verasonics Vantage 256	VisualSonicsVevo 770
Transducer type	128-element linear array	Single-element
Center frequency	5MHz	30MHz
Field of View	35mm×37.88mm	12mm×12mm
Scanning sequence	Coherent compounding	ECG gating
PRF	8333Hz	8000Hz
RF sampling rate	20MHz	200MHz

TABLE III –

PHANTOM EXPERIMENTAL RESULTS

	Stiff to Soft (n=4)	Soft to Stiff (n=4)	Static
PWV$_{stiff}$ (m/s)	3.96+0.28	3.59±0.06	3.52
PWV$_{soft}$(m/s)	2.34±0.09	2.93±0.08	2.41
Interface error (mm)	4.67±0.73	3.64±0.14	-

TABLE IV –

PHANTOM EXPERIMENTAL RESULTS

	Aneurysmal aortas (n = 8)
$e_{boundary}$ (mm)	0.68 ± 0.44
Mean aneurysm length (mm)	4.81 ± 1.27
Relative error (%)	13.7 ± 3.7
PWV (m/sec)	2.39 ± 1.41
Mean nr. of segments	3.6 ± 0.5